Requirements for coregistration accuracy in on-scalp MEG

Rasmus Zetter[a,*], Joonas Iivanainen[a], Matti Stenroos[a], Lauri Parkkonen[a,b]

[a] *Department of Neuroscience and Biomedical Engineering, Aalto University School of Science, FI-00076 Aalto, Finland*
[b] *Aalto NeuroImaging, Aalto University, FI-00076 Aalto, Finland*

Abstract

Optically-pumped magnetometers (OPMs) have recently reached sensitivity levels that enable their use in magnetoencephalography (MEG). In contrast to the SQUID sensors used in current MEG systems, OPMs do not require cryogenic cooling and can thus be placed within millimetres from the head, enabling the construction of *on-scalp* sensor arrays that conform to the shape of the head. To properly estimate the location of neural sources within the brain, one must accurately know the position and orientation of sensors in relation to the head. With the adaptable on-scalp MEG sensor arrays, this coregistration becomes more challenging than in current SQUID-based MEG systems that use rigid sensor arrays.

Here, we used simulations to quantify how accurately one needs to know the position and orientation of sensors in an on-scalp MEG system, and how different types of localisation errors affect forward modelling and source estimates obtained by minimum-norm estimation and dipole fitting.

We found that sensor position errors generally have a larger effect than orientation errors and that these errors affect the localisation accuracy of superficial sources the most. Based on our results, we propose < 4-mm RMS sensor position and < 10° RMS sensor orientation error levels as a requirement for source estimation with the above-mentioned methods in on-scalp MEG to obtain similar or higher accuracy than with current SQUID-based MEG systems.

Keywords: magnetoencephalography, optically-pumped magnetometer, coregistration

1. Introduction

Magnetoencephalography (MEG) is a non-invasive functional neuroimaging method for investigating electric neuronal activity inside the living human brain (Hämäläinen et al., 1993). MEG functions by measuring the magnetic field produced by neural currents in the brain using sensors positioned around the head. The MEG signal is complementary to that of electroencephalography (EEG), in which the potential distribution caused by neural activity is measured using electrodes placed on the scalp.

So far, the magnetometer employed for MEG has almost exclusively been the low-T_c superconducting quantum interference device (SQUID). These sensors require a cryogenic temperature that is typically attained by immersing SQUIDs in liquid helium ($T \approx 4.2$ K ≈ -269°C). The necessary thermal insulation keeps SQUIDs at least 2 cm away from the scalp and makes the construction of adaptable sensor arrays extremely challenging. Since sensitivity and spatial resolution are related to the distance between the sources and the sensors, the need of cryogenics eventually results in a considerable loss of signal amplitude and spatial resolution (Boto et al., 2016; Iivanainen et al., 2017). Since the sensor positions cannot be adapted to the head shape of individual subjects, the sensor–scalp-distance is further increased especially when measuring children and infants.

New sensor technologies with sensitivity high enough for MEG have emerged recently; optically-pumped magnetometers (OPMs) (Budker and Romalis, 2007; Budker and Kimball, 2013) and high-T_c SQUIDs (Öisjöen et al., 2012) hold promise as alternatives for low-T_c SQUIDs. These new sensor types do not require the same degree of

* Corresponding author.
Email address: rasmus.zetter@aalto.fi (Rasmus Zetter)

thermal insulation and can thus be placed much closer to the scalp, considerably boosting the sensitivity to neural sources. Especially the so-called zero-field OPMs that operate within the spin exchange relaxation-free (SERF) regime (Allred et al., 2002) appear promising as they offer high sensitivity while not requiring any cryogenics. Additionally, SERF OPMs can be miniaturised (Shah et al., 2007; Knappe et al., 2011), enabling the construction of high-density sensor arrays. SERF OPMs with sensitivities better than 5 $\mathrm{fT}/\sqrt{\mathrm{Hz}}$ have been demonstrated (Kominis et al., 2003; Griffith et al., 2010; Colombo et al., 2016; Knappe et al., 2016).

One could envision EEG-cap-like MEG sensor arrays utilising OPMs, in which the shape of the array conforms to the shape of the head. Recent simulation studies (Boto et al., 2016; Iivanainen et al., 2017) have shown these *on-scalp* MEG systems to have significantly higher sensitivity to neural sources compared to SQUID-based systems.

To be able to determine where in the brain the measured neuromagnetic signal originates (i.e. to perform source estimation), one needs to accurately know the position of sensors in relation to the head. In practice, source estimation is performed in conjunction with structural magnetic resonance images (MRI), enabling modelling of the head geometry at an individual level. For such modelling to be possible, the MEG data have to be coregistered with the MRI, i.e. the data from both modalities have to be transformed into a common coordinate system.

In current SQUID-based MEG systems, the sensors are rigidly mounted to the insert inside the cryogenic vessel, dewar. Thus, for coregistration, only the position and orientation of the subject's head in relation to the dewar need to be determined. In an on-scalp MEG system, coregistration becomes more challenging as each sensor needs to be individually localised with respect to the head. The nature of coregistration error also changes: in SQUID-based MEG systems, the coregistration error is mainly a systematic shift of the whole array, while in on-scalp MEG systems errors occur sensor-wise.

Coregistration for on-scalp MEG systems is similar to that for EEG, but in contrast to EEG, one needs to know the sensor orientation in addition to position. While the coregistration accuracy required for useful source estimation in EEG is agreed to be roughly < 5 mm (Brinkmann et al., 1998; Wang and Gotman, 2001; Koessler et al., 2007), the requirements for on-scalp MEG have so far been unexplored.

In this work, we determine how accurately one needs to know the sensor positions and orientations in on-scalp MEG systems for uncompromised forward and inverse modelling. We simulate a hypothetical OPM sensor array and investigate the effect of sensor-wise position and orientation error. We apply metrics that quantify the effect of this error on the forward models as well as metrics that quantify the performance of two common source estimation procedures, minimum-norm estimation and dipole modelling, in the presence of sensor localisation error.

2. Materials and methods

2.1. Anatomical models

T1-weighted magnetic resonance images were obtained from ten healthy adults (7 males, 3 females) using a 3T MRI scanner.The FreeSurfer software package (Dale et al., 1999; Fischl et al., 1999a; Fischl, 2012) was used for pre-processing the MRIs and for segmentation of the cortical surfaces.

For each subject, the surfaces of the skull and scalp were segmented using the watershed approach (Ségonne et al., 2004) implemented in FreeSurfer and MNE software (Gramfort et al., 2014). These surfaces were thereafter decimated to obtain three boundary element meshes (2 562 vertices per mesh). The neural activity was modelled as a primary current distribution constrained to the surface separating the cortical gray and white matter and discretised into a set of 10 242 current dipoles per hemisphere. For dipole modelling simulations, a sparser non-overlapping discretisation with 20 mm inter-source spacing was constructed. For minimum-norm estimation, sources were assumed to be normal to the local cortical surface, while for dipole modelling their orientation was not constrained. For visualisation and group-level statistics, individual brains were mapped to the average brain of the subjects using the spherical morphing procedure in FreeSurfer (Fischl et al., 1999b).

2.2. Forward models

The measured magnetic field $\mathbf{b}$ at the N_c sensors ($\mathbf{b} \in \mathbb{R}^{N_\mathrm{c}\times 1}$) is related to the source space $\mathbf{j} \in \mathbb{R}^{N_\mathrm{s}\times 1}$ by

$$\mathbf{b} = \mathbf{L}\mathbf{j}, \tag{1}$$

where $\mathbf{L}$ is the gain matrix ($\mathbf{L} \in \mathbb{R}^{N_c \times N_s}$) describing the sensitivity of each sensor to a unit source at each location in the source space. Each column i of $\mathbf{L} = [\mathbf{t}_1, \mathbf{t}_2, ...\mathbf{t}_{N_s}]$ represents the topography $\mathbf{t}_i$ of source i (how the sensors see that source), while each row j represents the sensitivity of sensor j to all sources.

Gain matrices were computed for each subject and sensor array using the linear Galerkin boundary element method (BEM) with an isolated source approach (ISA) as described by Stenroos and Sarvas (2012). The conductivities of the brain, skull and scalp compartments were set to $[1, \frac{1}{25}, 1] \cdot 0.33$ S/m, respectively.

2.3. Sensor models

Each OPM sensor was modelled as a set of eight discrete integration points. These were uniformly distributed within a cube-shaped sensitive volume with a side-length of 3 mm (see Table 1), representing the actual sensitive volume of the sensor. The output of each sensor was computed as the weighted sum of a single magnetic field component over the integration points. SQUID sensors comprised magnetometers (square pick-up loop with 25.8-mm side length) and planar gradiometers (loop size 26.4 mm, 16.8 mm baseline) as in the Elekta Neuromag® MEG systems (Elekta Oy, Helsinki, Finland); these sensors were modelled as in the MNE software (Table 1). SQUID and OPM magnetometers measured the z-component of the magnetic field in the local coordinates specified in Table 1, while the SQUID gradiometers measured a tangential derivative of the z-component.

Table 1: Sensor models. N is the number of integration points, $\mathbf{r}$ are their positions in a local coordinate system, and w are their respective weights.

Sensor type	N	$\mathbf{r}(x, y, z)$ [mm]	w
OPM	8	(± 0.75, ± 0.75, 0.75), (± 0.75, ± 0.75, 2.25)	1/8
SQUID magnetometer	4	(± 6.45, ± 6.45, 0.3)	1/4
SQUID gradiometer	2	(± 8.4, 0, 0.3)	± 1/16.8 mm

2.4. Sensor arrays

OPM sensor arrays were constructed using a subdivision approach in which a spherical surface was divided into horizontal levels. Each level was populated with sensors using equal angular spacing, except in the most anterior part of the head, for which smaller angular spacing was used to compensate for the non-spherical shape of the head. For the lowest levels, a gap was left for the face. This generalised sensor array was then projected onto the scalp surfaces of individual subjects.

The number of sensors per level and the inter-level distance was determined empirically so that the sensor array was maximally dense while still physically feasible for all 10 subjects. The feasibility was determined on the basis of a hypothetical sensor housing with a footprint of 20 x 20 mm^2 on the scalp. This criterion resulted in a sensor array consisting of 184 OPMs (Fig. 1).

The distance from the closest edge of the sensitive volume of the sensors to the scalp was set to 4.5 mm to leave space for a realistic sensor housing. The sensors were oriented to measure the normal component of the magnetic field with respect to the scalp, as this field component provides most information (Iivanainen et al., 2017).

From the original sensor array constructed for each subject, mis-coregistered sensor arrays with sensor-wise random position and orientation errors were constructed. The position of each sensor in a mis-coregistered array was sampled from a uniform distribution within a circle centred on the true sensor position. The circle was oriented tangentially to the scalp, and its radius represented the uncertainty in the measured position of the sensors. Radii were chosen so that the RMS position error was 2, 4 or 6 mm (corresponding to maximum sensor position errors of 2.8, 5.7 and 8.5 mm for the uniform distribution).

Furthermore, arrays with sensor-wise random orientation error were also constructed. In these arrays, each sensor was tilted from its true axis in a random direction. Error angles were sampled from a uniform distribution such that the RMS orientation error was 5°, 10° and 15° (corresponding to maximum orientation errors of 8.7°, 17.3° and 26.0°). Finally, to approximate more realistic scenarios, sensor arrays with both position and orientation error were constructed; these included arrays with 2-mm and 5°, 4-mm and 10° as well as 6-mm and 15° RMS errors.

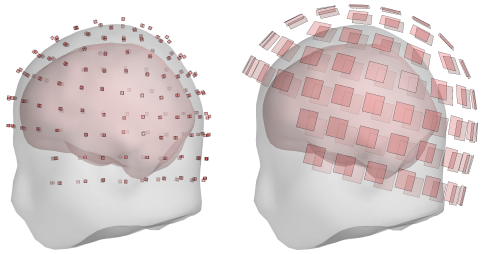

Figure 1: OPM (left) and SQUID (right) sensor arrays for one subject, showing the OPM sensitive volumes and SQUID pick-up loops.

For each simulated error level, 50 different mis-coregistered sensor arrays were constructed per subject, resulting in a grand total of 500 mis-coregistered sensor arrays per scenario. In the extremely rare case that the integration points of a mis-coregistered sensor came closer than 2 mm to the surface of the scalp, causing a risk of numerical inaccuracy, that sensor was moved outwards from the scalp to the minimum distance of 2 mm.

In addition to the OPM-based sensor arrays, a 306-channel (102 magnetometers, 204 planar gradiometers) SQUID-based Elekta Neuromag® MEG sensor array with the sensor-array position based on experimental MEG measurements was obtained for all subjects. These arrays, which did not include any coregistration errors, were used as the comparison baseline.

3. Metrics and computation

Several measures were used to quantify different aspects of the effect that mis-coregistration has both on the gain matrices (i.e. the forward models) and the source estimates calculated using these gain matrices (i.e. the inverse models). All metrics were calculated individually for each subject and each sensor array of that subject. Metrics were thereafter morphed to the average brain of the subjects and averaged. To keep metric results informative and avoid bias due to sources that are practically invisible in MEG, sources were split into deep and shallow categories (Fig. 2). Sources deeper than 30 mm from the inner surface of the skull were classed as deep while all others were classed as shallow. Thus, the majority of the cortex is classified as shallow, while deeper structures, from which the MEG signal is more unlikely to originate in, is classified as deep.

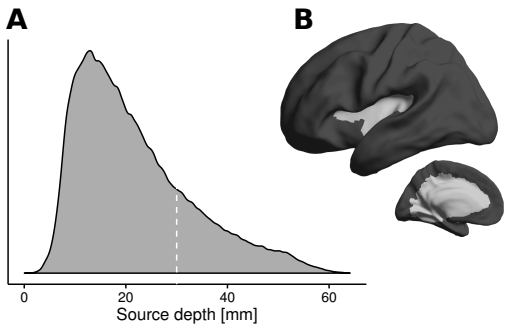

Figure 2: The depth of the cortical sources as measured from the inner surface of the skull. Data from all subjects pooled. A: Distribution as a density plot. The white dotted line represents the 30-mm threshold at which sources were split into shallow and deep. B: Average source depth thresholded to show which areas are classified as deep (light gray) and shallow (dark gray).

3.1. Forward metrics

Relative error (RE) is a general difference measure that is sensitive to changes in both amplitude and shape in the topographies. The relative error for the topography of a source is

$$\mathrm{RE} = \frac{|\mathbf{t}_{\mathrm{test}} - \mathbf{t}_{\mathrm{ref}}|}{|\mathbf{t}_{\mathrm{ref}}|}, \tag{2}$$

where $\mathbf{t}_{\text{ref}}$ and $\mathbf{t}_{\text{test}}$ are the reference and test topographies of the source, and $|\cdot|$ is the $l2$-norm. $\mathbf{t}_{\text{ref}}$ comes from the gain matrix of the original unperturbed sensor array, while $\mathbf{t}_{\text{test}}$ is from the gain matrix of a mis-coregistered sensor array.

To further investigate the errors in the shape of topographies due to mis-coregistration, the correlation coefficient (CC; Haueisen et al., 1997; Stenroos and Sarvas, 2012) between the topography in the reference sensor array and the corresponding topography in the erroneous sensor array was calculated for all individual sources. Unlike RE, this metric is insensitive to amplitude differences. CC is expressed as

$$\text{CC} = \frac{\mathbf{t}_{\text{ref}} - \bar{\mathbf{t}}_{\text{ref}}}{|\mathbf{t}_{\text{ref}} - \bar{\mathbf{t}}_{\text{ref}}|} \cdot \frac{\mathbf{t}_{\text{test}} - \bar{\mathbf{t}}_{\text{test}}}{|\mathbf{t}_{\text{test}} - \bar{\mathbf{t}}_{\text{test}}|}, \tag{3}$$

where $\cdot$ is the dot product, and $\bar{\mathbf{t}}$ denotes the mean of $\mathbf{t}$ across all sources.

3.2. Inverse metrics

Minimum-norm estimation

Minimum-$l2$-norm estimation (MNE) is a commonly used source estimation procedure (Dale and Sereno, 1993; Hämäläinen and Ilmoniemi, 1994) in which the minimisation of the $l2$-norm of the source estimate and the fidelity of the reconstruction of the measured signal are balanced. The source estimate $\tilde{\mathbf{j}}$ that satisfies the regularised minimum-$l2$-norm criterion is given by

$$\tilde{\mathbf{j}} = \mathbf{L}^{\text{T}}(\mathbf{L}\mathbf{L}^{\text{T}} + \lambda^2\mathbf{C})^{-1}\mathbf{b} \equiv \mathbf{G}\mathbf{b} \tag{4}$$

in which λ^2 is the regularisation parameter, $\mathbf{C}$ is the noise covariance matrix, and $\mathbf{G}$ is the resulting inverse operator. We used a diagonal noise covariance matrix $\mathbf{C}$, whose diagonal elements were proportional to the noise variances of the sensors. The numeric ratio between SQUID magnetometer and planar gradiometer noise variances was $(\frac{1}{100})^2$ (corresponding to 3 fT/$\sqrt{\text{Hz}}$ and 3 fT/($\sqrt{\text{Hz}}\cdot$cm), respectively).

We set the regularisation parameter as suggested by Lin and colleagues (2006):

$$\lambda^2 = \frac{tr(\tilde{\mathbf{L}}\tilde{\mathbf{L}}^T)}{N_{\text{c}}\,\overline{\text{SNR}}^2}, \tag{5}$$

where $\overline{\text{SNR}}$ is the assumed mean (amplitude) signal-to-noise ratio, N_{c} is the number of sensors, $tr(\cdot)$ is the trace operator, and $\tilde{\mathbf{L}} \equiv \mathbf{C}^{-1/2}\mathbf{L}$ is the whitened gain matrix. We set $\overline{\text{SNR}}^2$ to 9, the default value in MNE software.

We used the minimum-$l2$-norm estimates as the basis for several source localisation metrics. The measures used to investigate the effect of sensor localisation error on the minimum-$l2$-norm source estimates are based on the concept of resolution analysis as applied in earlier literature (Grave De Peralta Menendez et al., 1997; Molins et al., 2008; Hauk et al., 2011; Stenroos and Hauk, 2013; Iivanainen et al., 2017). In resolution analysis, metrics are derived from the resolution matrix

$$\mathbf{R} = \mathbf{G}\mathbf{L}, \tag{6}$$

where $\mathbf{G}$ is the inverse operator, here the MNE operator of Eq. 4. The columns of the resolution matrix $\mathbf{R}$ consist of point-spread functions (PSFs) $\mathbf{p} \in \mathbb{R}^{N_{\text{s}}\times 1}$, which describe how the activation of each source is distorted by the imaging system, i.e. how the activation of each source is seen in the source estimate. We computed the resolution matrix using the inverse operator based on each mis-coregistered sensor array together with the gain matrix of the original sensor array, thus simulating the effect of mis-coregistration.

We assessed the localisation performance of each sensor array by computing the peak position error (PPE) for all sources, which describes the displacement of the centre-of-mass of the PSF from the actual source position $\mathbf{r}_{\text{ref}}$ (Lin et al., 2006; Stenroos and Hauk, 2013; Iivanainen et al., 2017):

$$\text{PPE} = \left|\mathbf{r}_{\text{ref}} - \frac{\sum_i |\mathbf{p}_i|\mathbf{r}_i}{\sum_i |\mathbf{p}_i|}\right|. \tag{7}$$

When calculating the PPEs, we thresholded the PSFs by only including the source points at which $|\mathbf{p}_i| \geq 0.5 \cdot \mathbf{p}_{\text{max}}$, as was done by Stenroos and Hauk (2013).

The spatial spread of the source estimate was characterised by calculating the spatial deviation (SD) of the PSFs (Stenroos and Hauk, 2013):

$$\mathrm{SD} = \sqrt{\frac{\sum_i |\mathbf{p}_i|(\mathbf{r}_i - \mathbf{r}_{\mathrm{ref}})^2}{\sum_i |\mathbf{p}_i|}}. \tag{8}$$

When calculating the SD, we thresholded the PSFs in the same manner as when calculating the PPE.

Finally, as PPE only quantifies the localisation performance of the source estimator, we also computed the correlation between the PSFs of the original and mis-coregistered sensor arrays:

$$\mathrm{CC} = \frac{\mathbf{p}_{\mathrm{ref}} - \overline{\mathbf{p}}_{\mathrm{ref}}}{|\mathbf{p}_{\mathrm{ref}} - \overline{\mathbf{p}}_{\mathrm{ref}}|} \cdot \frac{\mathbf{p}_{\mathrm{test}} - \overline{\mathbf{p}}_{\mathrm{test}}}{|\mathbf{p}_{\mathrm{test}} - \overline{\mathbf{p}}_{\mathrm{test}}|}, \tag{9}$$

which quantifies the effect of mis-coregistration on the shape of the point-spread functions.

Dipole modelling

We implemented a least-squares single dipole localisation using a simple grid search procedure. The same source space as in the MNE resolution analysis was used as the search space for dipole modelling, but the data were generated using a different simulation source space with non-overlapping discretisation, each source of which was activated separately. To keep the computation time reasonable, the simulation source space was sparser, with a inter-source spacing of 20 mm. The simulated sources were oriented normally to the local cortical surface, but the source orientation was a free parameter in the dipole modelling procedure.

White Gaussian noise was added to the simulated magnetic field to approximate sensor noise. For the SQUID arrays, the noise characteristics of the Elekta Neuromag® MEG system were used: the spectral noise densities for SQUID magnetometers and planar gradiometers were set to 3 $\mathrm{fT}/\sqrt{\mathrm{Hz}}$ and 3 $\mathrm{fT}/(\sqrt{\mathrm{Hz}} \cdot \mathrm{cm})$, respectively. For the OPMs, three different noise levels were used:

1. 3.0 $\mathrm{fT}/\sqrt{\mathrm{Hz}}$, which is equal to that of current SQUID magnetometers.
2. 7.4±0.6 $\mathrm{fT}/\sqrt{\mathrm{Hz}}$, which is the subject-specific break-even noise density at which the SQUID magnetometers and OPMs would have equal SNR (the mean across all cortical sources in the simulation source space).
3. 15 $\mathrm{fT}/\sqrt{\mathrm{Hz}}$, which is demonstrated with current commercial SERF OPMs.

The source amplitude for a given SNR and noise level was determined using the definition of the local SNR for source i given by Goldenholz and colleagues (2009):

$$\mathrm{SNR}_i^2 = \frac{a^2}{N_{\mathrm{c}}} \sum_{j=1}^{N_{\mathrm{c}}} \frac{\mathbf{t}_{j,i}^2}{\sigma_j^2}, \tag{10}$$

where a^2 is the source variance, N_{c} is the number of sensors, and σ_j^2 is the noise variance of sensor j. In the case of white noise, the noise variance can be expressed in terms of the spectral noise density n and bandwidth BW, $\sigma_j^2 = n_j^2 \mathrm{BW}$. The source variance that produced a mean SNR^2 of 10 over all sources for the SQUID magnetometer array was used in all simulations, and the bandwidth was set to 40 Hz. To treat both SQUID sensor types of the 306-channel array equally, the gain matrix was whitened before applying it to the data.

To simulate the effect of mis-coregistration, the simulated magnetic field was computed using the gain matrix of the original sensor array while the gain matrix of a mis-coregistered sensor array was used for the dipole modelling procedure.

We quantified the impact of mis-coregistration using dipole localisation error (DLE), i.e. the three-dimensional Euclidean distance between the fitted and actual dipoles. In a similar manner, we defined dipole orientation error (DOE) as the difference in orientation between the actual and fitted dipoles. Finally, we compared the goodness-of-fit (GOF), i.e. how well the fitted dipoles explain the original data:

$$\mathrm{GOF} = 1 - \frac{|\mathbf{b}_{\mathrm{fit}} - \mathbf{b}_{\mathrm{meas}}|^2}{|\mathbf{b}_{\mathrm{meas}}|^2}, \tag{11}$$

where $\mathbf{b}_{\mathrm{meas}}$ is the measured magnetic field and $\mathbf{b}_{\mathrm{fit}}$ is the magnetic field produced by the fitted dipole. The GOF is widely used as an indicator of the appropriateness of a dipole model.

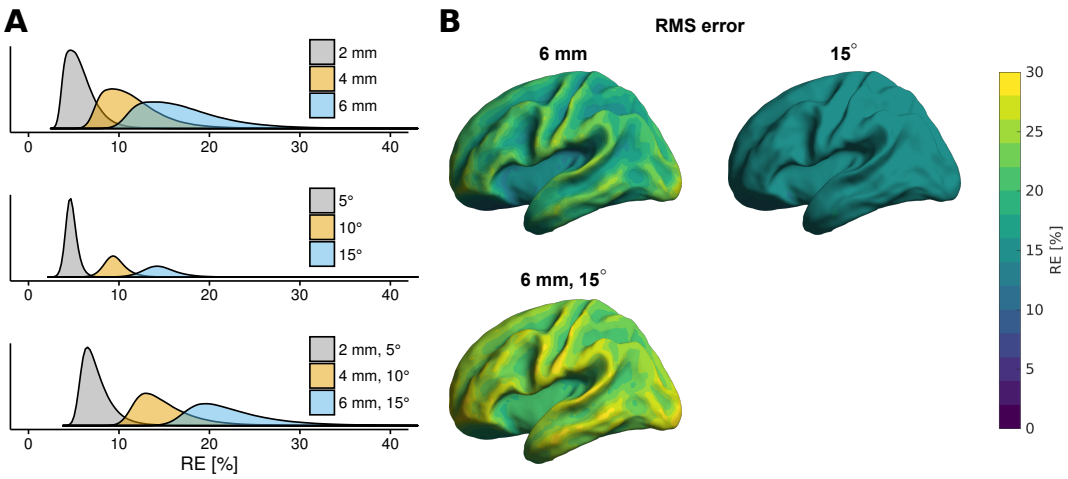

Figure 3: Relative error of topographies over all subjects at different levels of sensor position and orientation error. A: Error distributions shown as density plots. B: The mean RE over all subjects at the highest error level.

4. Results

4.1. Forward metrics

The relative error of topographies due to the random sensor position error is shown in Table 2 and Fig. 3. This error is largest in superficial areas, which is to be expected as these areas are closer to the sensors. Similarly, the shapes of the source topopgraphies are most affected in superficial areas (Fig. A1, Table 2). Unlike the sensor-wise position error, random orientation error is manifested throughout the cortex regardless of source location and depth (Fig. 3, Table 2). Similar effects can be seen in the shapes of the topographies, although the CCs are not affected to the same degree as the REs (Fig. A1). When sensor position and orientation errors are present simultaneously, the effects of these errors add up in a sub-linear manner (Fig. 3).

4.2. Inverse metrics

Minimum-norm estimation

Peak position errors (PPEs) and correlation coefficients (CCs) of PSFs are summarised in Table 3. The average PPE over all subjects (Fig. 4, Table 3) is very large for deep sources, of the order of several centimetres, regardless of the amount of sensor position error. The PPEs for shallow sources are much smaller, but are considerable also

Table 2: Mean relative errors and correlation coefficients of source topographies with different levels of sensor-wise position and orientation error.

RMS sensor-wise error		Shallow sources		Deep sources	
Position [mm]	Orientation [°]	RE [%]	CC [%]	RE [%]	CC [%]
2	0	6.1	99.7	4.3	99.9
4	0	12.2	98.8	8.7	99.4
6	0	18.1	97.4	13.0	98.7
0	5	4.8	99.9	4.7	99.9
0	10	9.7	99.5	9.4	99.6
0	15	14.7	98.9	14.3	99.0
2	5	7.8	99.7	6.4	99.8
4	10	15.6	98.7	12.8	99.2
6	15	23.2	97.2	19.3	98.1

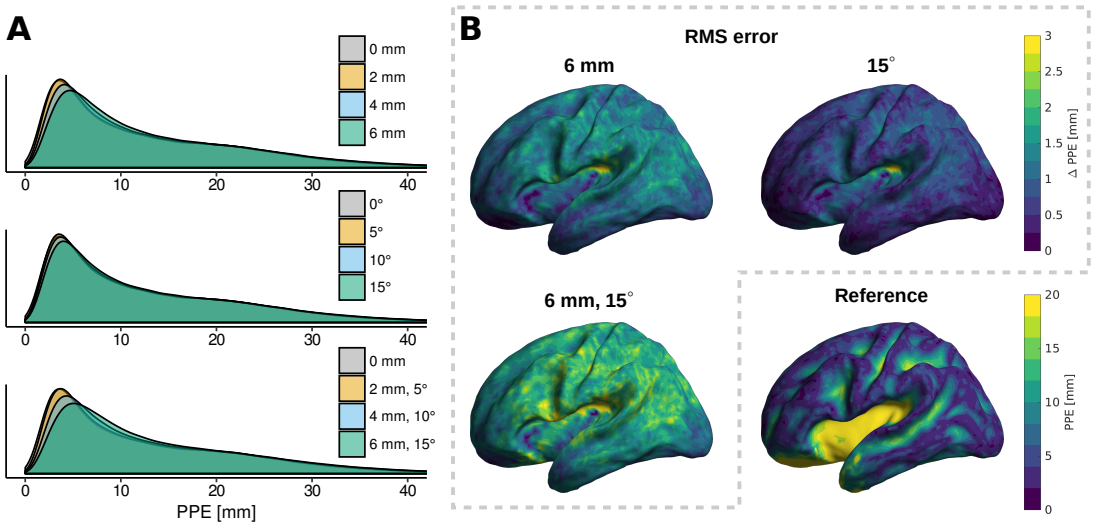

Figure 4: Average peak position error (PPE) of PSFs over all subjects in the presence of different levels of sensor-wise position and orientation error. A: Error distributions as density plots. B: The mean difference in PPE between the extrema of the error levels, and the PPE for the reference with no error.

when no sensor position error is present. The increase in PPE due to sensor position error is seen both in shallow and deep areas of the cortex, although it is proportionally much larger in shallow areas.

Without mis-coregistration, the PPEs of the OPM array are smaller than those of the reference SQUID arrays, i.e., the 306-channel "All-SQUID" array and the 102-channel magnetometer-only "Mag-SQUID" array (Table 3). The difference diminishes when a small amount of mis-coregistration is present. When the OPM array had both 6-mm and 15° RMS position and orientation errors, the PPEs were larger than those for either SQUID array.

The PSFs spread due to mis-coregistration as quantified by the SD metric (Fig. 6). This spreading is most pronounced in the areas of high sensitivity. For deep sources, sensor orientation vs. position error causes a proportionately larger SD increase. The SD values of the 102-channel SQUID magnetometer array are much larger than those of the 306-channel SQUID array, which in turn has larger SD values than the OPM array.

Fig. 5 shows the correlations of the PSFs obtained with different sensor position and orientation errors. In concordance with the errors in the forward model, superficial areas are affected the most by position error. While the orientation error had a global effect on the forward models, it affects the MNE mostly in the superficial areas.

Table 3: PPEs, SDs and CCs of point-spread functions computed from the MNE resolution matrix.

Sensor type	RMS sensor-wise error		Shallow sources			Deep sources		
	Position [mm]	Orientation [°]	PPE [mm]	SD [mm]	CC [%]	PPE [mm]	SD [mm]	CC [%]
OPM	0	0	8.7	15.9	-	26.0	37.7	-
Mag-SQUID	0	0	9.7	21.3	-	27.0	39.8	-
All-SQUID	0	0	9.2	19.2	-	26.3	38.9	-
OPM	2	0	8.9	16.1	99.5	26.3	38.0	99.9
	4	0	9.2	16.7	98.1	26.7	38.7	99.5
	6	0	9.7	17.5	95.9	27.1	39.6	98.9
	0	5	8.8	16.0	99.7	26.2	38.0	99.9
	0	10	9.0	16.4	98.8	26.5	38.9	99.7
	0	15	9.4	17.0	97.5	26.8	40.4	99.2
	2	5	8.9	16.2	99.2	26.4	38.3	99.8
	4	10	9.5	17.1	97.0	26.9	49.8	99.2
	6	15	10.2	17.3	93.7	27.4	41.6	98.2

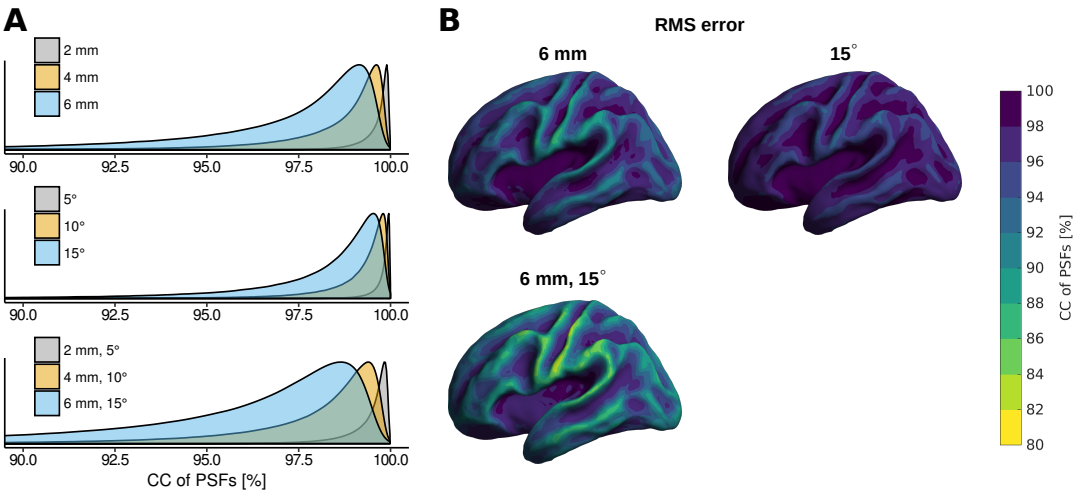

Figure 5: The distibution of correlation coefficients (CCs) for point-spread functions (PSFs) over all subjects at different levels of sensor position and orientation error. A: Distributions shown as density plots. For easier visualisation, the densities are normalised to the same maximum value. B: The mean CCs of PSFs over all subjects at the highest error levels.

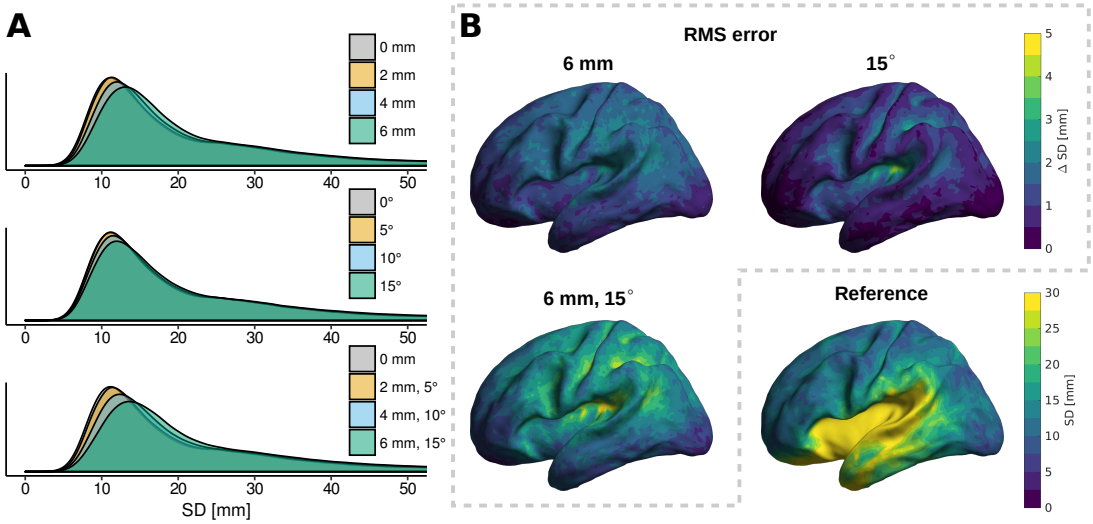

Figure 6: Average spatial deviation (SD) of PSFs over all subjects in the presence of different levels of sensor-wise position and orientation error. A: Distributions as density plots. B: The mean difference in SD compared to the reference array over all subjects at the highest error levels.

Dipole modelling

When using the same noise density of 3 $\mathrm{fT}/\sqrt{\mathrm{Hz}}$ for both SQUID magnetometers and OPMs, the SNR^2 for the OPMs was 61.6±10.4 (mean±standard deviation across the subjects). Metrics for this scenario are shown in Table 4. The increased SNR resulted in much larger GOF values and moderately smaller DLEs and DOEs. Even with substantial mis-coregistration, the DLEs for the OPM array remain smaller than for either SQUID array.

The results for the scenario in which the noise density of the OPMs was set so that the SNR^2 would be equal to that of the SQUID magnetometers are presented in Table A1. GOF values are roughly equal for OPM and SQUID magnetometer arrays, with GOF values of the 306-channel SQUID array being substantially higher. In spite of this, the DLEs and DOEs for the OPM array were smaller for shallow sources than for either SQUID array at all tested levels of mis-coregistration.

Fig. 7 and Table 5 show the dipole modelling results for the simulation scenario where the OPM noise den-

sity was set to 15 fT/$\sqrt{\text{Hz}}$, resulting in the OPM SNR^2 of 2.47±0.42 (Eq. 10, mean±standard deviation across the subjects). The large difference in the SNRs between the SQUID and OPM sensor arrays is clearly seen in the GOF values. In spite of this large discrepancy in SNRs, the dipole localisation accuracy of the OPM sensor array is approximately on par with the 306-channel SQUID array when no mis-coregistration is present. Furthermore, the OPM array has superior localisation accuracy compared to the 102-channel SQUID magnetometer array, even with substantial mis-coregistration.

Dipole position errors of $\lesssim$ 10 mm are attainable for superficial sources at all sensor position error levels included in the simulations and at all simulated noise levels. The sensor position error has a larger effect on the localisation performance than the orientation error, although the cumulative effect of both error types is even higher. The GOF values are highly affected by source depth and SNR, while mis-coregistration only has a small effect on them.

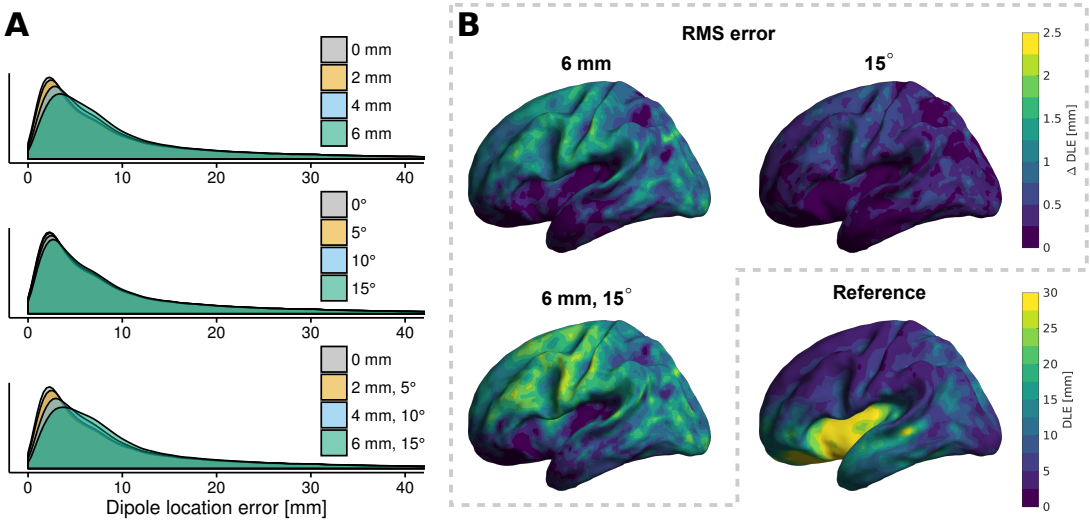

Figure 7: Average DLE over all subjects in the presence of different levels of mis-coregistration when OPMs had a noise density of 15 fT/$\sqrt{\text{Hz}}$. A: Distributions shown as density plots. B: The mean difference in DLE compared to the reference array over all subjects at the highest error level.

Table 4: Mean metrics related to the dipole fitting procedure at different levels of sensor position and orientation error when both OPMs and SQUID magnetometers had a noise density of 3 fT/$\sqrt{\text{Hz}}$ and SQUID gradiometers had a noise density of 3 fT/($\sqrt{\text{Hz}}\cdot$cm).

Sensor type	RMS sensor-wise error		Shallow sources			Deep sources		
	Position [mm]	Orientation [°]	DLE [mm]	DOE [°]	GOF [%]	DLE [mm]	DOE [°]	GOF [%]
OPM	0	0	7.3	35.3	89.4	15.7	30.3	64.7
Mag-SQUID	0	0	12.6	51.3	80.7	26.3	56.3	54.2
All-SQUID	0	0	10.3	45.7	90.1	19.0	44.2	79.8
OPM	2	0	7.5	36.5	89.1	15.8	31.4	64.5
	4	0	7.8	39.0	88.3	15.9	31.6	64.2
	6	0	8.3	41.9	86.9	16.1	32.0	63.6
	0	5	7.4	35.8	89.2	15.8	31.4	64.5
	0	10	7.5	36.7	88.8	15.8	31.4	64.1
	0	15	7.7	38.5	87.9	15.9	31.7	63.5
	2	5	7.5	36.8	89.0	15.8	31.4	64.4
	4	10	7.9	39.8	87.7	16.0	31.7	63.7
	6	15	8.5	43.4	85.5	16.2	32.3	62.5

Table 5: Mean metrics related to the dipole fitting procedure at different levels of sensor position and orientation error when OPMs had a noise density of 15 fT/$\sqrt{\text{Hz}}$, SQUID magnetometers had a noise density of 3 fT/$\sqrt{\text{Hz}}$ and SQUID gradiometers had a noise density of 3 fT/($\sqrt{\text{Hz}}\cdot$cm).

Sensor type	RMS sensor-wise error		Shallow sources			Deep sources		
	Position [mm]	Orientation [°]	DLE [mm]	DOE [°]	GOF [%]	DLE [mm]	DOE [°]	GOF [%]
OPM	0	0	9.7	46.7	59.8	30.7	59.3	19.9
Mag-SQUID	0	0	12.6	51.3	80.7	26.3	56.3	54.2
All-SQUID	0	0	10.3	45.7	90.1	19.0	44.2	79.8
OPM	2	0	9.8	46.6	59.6	30.7	59.6	19.7
	4	0	10.1	48.1	59.0	30.9	60.2	19.6
	6	0	10.6	50.1	58.1	31.1	60.5	19.5
	0	5	9.7	46.2	59.6	30.9	59.6	19.7
	0	10	9.9	46.7	59.3	31.0	59.7	19.6
	0	15	10.1	47.7	58.8	31.2	60.0	19.4
	2	5	9.9	46.8	59.5	31.0	59.6	19.6
	4	10	10.3	48.6	58.6	31.3	60.2	19.5
	6	15	10.8	51.0	57.2	31.6	60.7	19.2

5. Discussion

In this study, we have investigated the effects of mis-registration of on-scalp MEG sensors on the forward model and source estimation. We found superficial sources to be affected more than deeper ones. We also discovered that the effect of sensor position error was larger than that of the sensor orientation. According to our results, RMS sensor position errors of < 4 mm cause a < 7% increase in any of our source estimation error metrics for either MNE or dipole modelling. Thus, coregistration should not pose a major problem in the adoption of on-scalp MEG as long as modern, accurate coregistration methods are used.

5.1. Simulation methodology

We designed our simulations according to actual, commercially available OPMs (QuSpin Inc., Louisville CO, USA); the stand-off distance and dimensions of the OPM sensor housing and sensitive volume represented those of these sensors. The hypothetical sensor array was constructed to be maximally dense while still fitting the heads of all 10 adult subjects. The assumed 20 x 20 mm^2 scalp footprint of each sensor is a conservative estimate of current OPM casing; the SERF OPMs by QuSpin have dimensions of 13 x 19 mm^2, and smaller yet sufficiently sensitive sensor designs have also been demonstrated (e.g. Sander et al., 2012; Alem et al., 2014).

The noise density of 15 fT/$\sqrt{\text{Hz}}$ used for the OPMs in the dipole modelling simulations was also based on the OPM sensor by QuSpin. For the Elekta Neuromag® SQUID-based MEG system, we assumed 3 fT/$\sqrt{\text{Hz}}$ for the magnetometers and 3 fT/($\sqrt{\text{Hz}}\cdot$cm) for the gradiometers, which are typical values for this system.

The source estimation methods selected for this study represent two very different approaches: minimum-norm estimation sets a general, weak prior, while dipole modelling uses a very strong assumption of the primary current distribution underlying the measured data. Compared to dipole modelling, MNE is less accurate in localizing focal sources but appears more robust to coregistration and other errors, while dipole modelling is more sensitive to errors in the forward model (Stenroos and Hauk, 2013). In the dipole localisation simulations, separate and non-overlapping source spaces were used for data simulation and source estimation. In this way, any bias that could be caused by using the same source space for simulation and estimation was avoided. This procedure also sets a lower bound for the dipole localisation error. The closest point in the estimation source space to the simulation source space was on average 1.3±0.6 mm (mean±standard deviation).

When conducting the simulations, the possibility of intersecting or below-scalp sensor housings was not taken into account as this situation can happen in reality if sensor position or orientation measurement error is present. However, such a "sanity check" should be implemented in real coregistration procedures to ensure that the measured sensor positions are reasonable. In particular, if the sensitive volume intersects the head surface, forward modelling may produce large errors. In this study, we moved a sensor outwards to a minimum distance of 2 mm if any of its integration points was closer to the scalp than 2 mm. This phenomenon occurred extremely rarely as there were less than 20 such occurences in all simulations.

5.2. Effects of sensor position and orientation errors

Generally, random sensor orientation error produces less adverse effects than position error both on the forward models and source estimation results. Unlike the position error, orientation error affects the forward model throughout the source space regardless of source position or depth. Additionally, sensor orientation errors mostly affected the RE rather than CC values, suggesting that orientation errors primarily alter amplitudes rather than the shapes of topographies. This phenomenon did not directly translate to either source estimation method included in this study; sensor orientation error mostly affected shallow sources rather than having a global effect.

The localisation performance of MNE for the simulated focal sources is modest with both the OPM and SQUID arrays as demonstrated by the PPE metric, which is never below 5 mm, even without any mis-coregistration. Regardless of the localisation accuracy of MNE, on-scalp MEG systems possess higher spatial resolution than conventional SQUID-based MEG systems, as also seen by the lower SD values in the current work. Similar findings were also reported by Iivanainen and colleagues (2017).

The higher source localisation performance of the OPM sensor array in comparison to the SQUID arrays was also manifested in the dipole modelling simulations; the DLE was consistently smaller for OPM arrays even with substantial sensor position error. This result was in spite of the much lower SNR that was present for the OPM arrays. When the OPM noise density was set equal to that of current SQUID magnetometers, the SNR of the OPMs was very high, providing a modest improvement in dipole localisation accuracy.

5.3. Requirements for sensor localisation accuracy

Since the SNR of MEG diminishes with increasing source depth, shallow neocortical sources typically dominate MEG. Therefore, in the following we focus on the results for shallow sources. Based on the results of both MNE and dipole modelling simulations, an RMS sensor position error of 4 mm causes an increase in source localisation error of 5% for the MNE simulations (change in PPE) and 7% for the dipole modelling simulations (change in DLE, OPM noise density: 3 $\mathrm{fT}/\sqrt{\mathrm{Hz}}$) over a scenario with error-free coregistration. We also included simulations scenarios in which both position and orientation errors were present. For example, combined 2-mm and 5° RMS errors had < 3% effect on sensor localisation accuracy for either tested source estimation method. However, RMS errors of 4 mm and 10° increased source localisation errors by 10% and 8% for MNE and dipole modelling, respectively.

Ultimately, it is up to the user to decide how accurate source estimates are needed and, by extension, how large sensor position and orientation errors can be tolerated. Nevertheless, on the basis of our simulation results with MNE and dipole modelling, we propose 4-mm sensor position and 10° sensor orientation RMS errors as a general guideline for the maximum acceptable mis-coregistration for whole-head on-scalp MEG systems. When coregistration errors are smaller than these requirements, the on-scalp MEG system performed at or above the level of conventional SQUID-based MEG systems. With larger mis-coregistration errors, the advantage of on-scalp MEG may be lost.

These guideline requirements are appropriate for the inverse modelling techniques presented in this study. Compared to those techniques, distributed source estimates which pose strong priors, typically sparsity of the estimate, may be more sensitive to mis-coregistration. These methods include minimum-$l1$-norm estimation (Matsuura and Okabe, 1995; Uutela et al., 1999), mixed-norm estimation (Ou et al., 2009; Gramfort et al., 2012), techniques utilising multivariate source prelocalisation (Mattout et al., 2005) and different beamformer variants (Van Veen et al., 1997; Huang et al., 2004).

Interference suppression techniques based on the physics of the measurement, such as the signal-space separation (SSS) method (Taulu and Kajola, 2005) and variations thereof, may also have stricter coregistration requirements. For example, Nurminen and colleagues (2008) showed that accurate knowledge of array geometry was necessary for both SQUID magnetometer and axial gradiometers arrays to reach high suppression factors against external magnetic field sources when using SSS. Additionally, they reported that these accuracy requirements are likely to be even stricter for sensor arrays capable of measuring higher spatial frequencies, such as on-scalp MEG systems.

5.4. Sensor localisation methods

In light of our results, most of the sensor localisation methods that have been applied in MEG and EEG seem accurate enough also for on-scalp MEG; these methods yield < 4-mm RMS errors in a head-sized volume when

used with care. For example, the Polhemus® 3D electromagnetic digitiser system (Polhemus Inc., Colchester, VT, USA) has a reported accuracy of 3–7 mm (e.g. Koessler et al., 2010; Baysal and Şengül, 2010; Dalal et al., 2014). Methods more accurate than the Polhemus® system exist, especially the recently-developed optical ones such as photogrammetry (e.g. Bauer et al., 2000; Russell et al., 2005) and structured-light scanning techniques (e.g. Koessler et al., 2011; Ettl et al., 2013; Hironaga et al., 2014). However, other factors such as cost, ease of use, coverage, and speed may be the decisive factors in choosing the method to be used. For example, the Polhemus ® system requires the operator to move a digitiser stylus to every sensor, making coregistration more laborious and error-prone, especially if one needs to digitise the sensor orientation as well. To its benefit, the Polhemus system is proven to work reliably and is widely used for coregistration for both EEG and MEG. Optical surface mapping methods, on the other hand, have the potential to be fast (Koessler et al., 2011) or even instantaneous (Bauer et al., 2000) depending on the implementation. When using optical methods, one needs to identify the individual sensors non-ambiguously. In spite of this complication, optical surface mapping methods seem a very promising solution, as they can collect large amounts of surface data, including the shape of the head and face, very quickly (Koessler et al., 2011). This complementary information can be exploited in coregistration with the MR-image.

In SQUID-based MEG, the Polhemus® system is the most widely used coregistration method, although some developments using the methods described above have taken place; optical scanning systems have been applied to MEG (Bardouille et al., 2012; Hironaga et al., 2014; Murthy et al., 2014), as well as individualised head casts that snugly fit between the head of the subject and the helmet-shaped cavity of the dewar(Troebinger et al., 2014; Meyer et al., 2017). Similar efforts have been devoted to OPM-based on-scalp MEG by Boto and colleagues (2017), who used a head cast for both coregistration purposes and to physically support the sensors.

5.5. Sources of model error

Sensor localisation is just one part of the coregistration process and thus not the only source of coregistration error. Once the position and orientation of the sensors and some head surface points (e.g. fiducials) are known in a common coordinate system, the surface points are typically fitted to MR-images. A variety of methods for this fitting procedure exist, e.g. adaptations of the Levenberg–Marquardt algorithm (Kozinska et al., 1997, 2001) and the ICP algorithm (Besl and McKay, 1992). Coregistration procedures using solely the standard anatomical landmarks (the nasion and the preaurical points; Jasper, 1958) are considered to be less accurate than those that additionally use dense head surface data (Whalen et al., 2008). In the current study, mis-coregistration was attributed exclusively to errors in the measurement of sensor position and orientation.

Other significant types of errors in the forward solution include the level of detail and geometric errors in the head model and errors in conductivity values. In general, the MEG forward model is not highly sensitive to the resistivity of the skull: it has been shown (Stenroos and Nummenmaa, 2016) that skull conductivity can be over- or underestimated by a factor of 1.5 without causing RE > 1% for SQUID arrays. The previous comparison does not take into account the effect of the CSF, whose omission in a BEM head model can result in an RE of up to ~20% when compared to a model including the CSF (Stenroos and Nummenmaa, 2016).

5.6. Prospects

To date, several research groups as well as commercial entities have developed OPMs that can be and have been applied to MEG both in humans (e.g. Shah and Wakai, 2013; Johnson et al., 2013) and animals (Alem et al., 2014). The sensors and experimental set-ups vary from single-channel measurements using physically very large magnetometers (e.g. Xia et al., 2006; Kamada et al., 2015) to compact sensors (e.g. Shah and Wakai, 2013; Knappe et al., 2014) that could feasibly be deployed in a sensor array covering the entire scalp. Even though single sensors theoretically suitable for a high-density whole-head array have been developed, no such system has been demonstrated yet. Remaining challenges, apart from coregistration, include shielding and sensor cross-talk as well as total system cost. An additional practical challenge for OPM-based MEG is sturdy but adjustable mechanical support for a high-density OPM sensor array. Using a cap as in EEG might be viable, but it remains to be seen if such a solution provides enough mechanical support for OPMs, which are substantially heavier and larger than EEG electrodes and are sensitive to changes in their orientation.

6. Conclusions

In this work, we investigated the effect of errors in determining sensor positions and orientations in on-scalp MEG arrays. We found that position error introduces larger errors in the forward model and hampers source estimation performance more than the orientation error does. Based on our results, we propose < 4-mm RMS position and < 10° RMS orientation error levels as a general-purpose requirement for source estimation in on-scalp MEG. Current coregistration methods used in both EEG and MEG perform at or above this level; thus, coregistration should not pose a large problem to the adoption of on-scalp MEG. Yet, there is a need for a faster, more reliable and practical method for determining on-scalp MEG sensor positions and orientations.

Acknowledgements

The authors thank the Advanced Magnetic Imaging centre of Aalto Neuroimaging Infrastructure for the MR images and Aalto University Science-IT for providing computational resources. Research reported in this publication received funding from the European Research Council under ERC Grant Agreement n. 678578 and the National Institute of Neurological Disorders and Stroke of the National Institutes of Health under Award Number R01NS094604. The content is solely the responsibility of the authors and does not necessarily represent the official views of the funding organisations.

Appendix

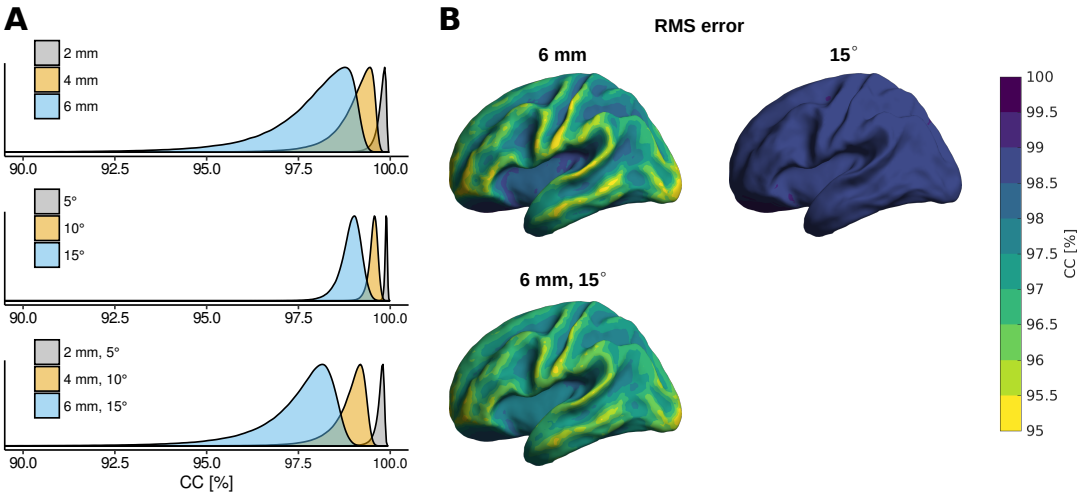

Figure A1: Average correlation coefficients (CCs) of source topographies over all subjects in the presence of different levels of sensor-wise position and orientation error. A: Distributions shown using density plots. For easier visualisation, the densities are are normalised to the same maximum value. B: For more detailed visualisation, the mean CCs over all subject in the most extreme cases of each scenario type are also visualised in the form of inflated brain atlases.

Table A1: Mean metrics related to the dipole fitting procedure at different levels of sensor position and orientation error when the noise density of OPMs was set so that their SNR was equal to that of SQUID magnetometers. SQUID magnetometers had a noise density of 3 fT/$\sqrt{\text{Hz}}$ and SQUID gradiometers had a noise density of 3 fT/($\sqrt{\text{Hz}}\cdot$cm). The resulting noise density for the OPMs was 7.4±0.6 fT/$\sqrt{\text{Hz}}$.

Sensor type	RMS sensor-wise error		Shallow sources			Deep sources		
	Position [mm]	Orientation [°]	DLE [mm]	DOE [°]	GOF [%]	DLE [mm]	DOE [°]	GOF [%]
OPM	0	0	7.9	38.5	80.3	20.3	39.1	41.2
Mag-SQUID	0	0	12.6	51.3	80.7	26.3	56.3	54.2
All-SQUID	0	0	10.3	45.7	90.1	19.0	44.2	79.8
OPM	2	0	8.0	39.1	80.0	20.2	40.1	40.9
	4	0	8.3	41.3	79.3	20.2	40.2	40.7
	6	0	8.8	44.0	78.0	20.4	40.7	40.4
	0	5	7.9	38.5	80.1	20.1	39.9	40.9
	0	10	8.1	39.3	79.7	20.2	39.7	40.7
	0	15	8.2	40.8	79.0	20.3	40.3	40.3
	2	5	8.0	39.4	79.9	20.2	39.9	40.9
	4	10	8.5	42.0	78.7	20.4	40.2	40.4
	6	15	9.0	45.3	76.8	20.6	41.0	39.7

References

Alem, O., Benison, A. M., Barth, D. S., Kitching, J., and Knappe, S. (2014). Magnetoencephalography of epilepsy with a microfabricated atomic magnetrode. *Journal of Neuroscience*, 34(43):14324–14327.

Allred, J. C., Lyman, R. N., Kornack, T. W., and Romalis, M. V. (2002). High-Sensitivity Atomic Magnetometer Unaffected by Spin-Exchange Relaxation. *Physical Review Letters*, 89(13):130801.

Bardouille, T., Krishnamurthy, S. V., Hajra, S. G., and Darcy, R. C. N. (2012). Improved localization accuracy in magnetic source imaging using a 3-D laser scanner. *IEEE Transactions on Biomedical Engineering*, 59(12):3491–3497.

Bauer, H., Lamm, C., Holzreiter, S., Holländer, I., Leodolter, U., and Leodolter, M. (2000). Measurement of 3D electrode coordinates by means of a 3D photogrammetric head digitizer. *NeuroImage*, 11(5):S461.

Baysal, U. and Şengül, G. (2010). Single Camera photogrammetry system for EEG electrode identification and localization. *Annals of Biomedical Engineering*, 38(4):1539–1547.

Besl, P. and McKay, N. (1992). A Method for Registration of 3-D Shapes. *IEEE Transactions on Pattern Analysis and Machine Intelligence*, 14(2):239–256.

Boto, E., Bowtell, R., Kruger, P., Fromhold, M. T., Morris, P. G., Meyer, S. S., Barnes, G. R., and Brookes, M. J. (2016). On the Potential of a new generation of Magnetometers for MEG: a Beamformer Simulation Study. *PLoS ONE*, 11:1–24.

Boto, E., Meyer, S. S., Shah, V., Alem, O., Knappe, S., Kruger, P., Fromhold, T. M., Lim, M., Glover, P. M., Morris, P. G., Bowtell, R., Barnes, G. R., and Brookes, M. J. (2017). A new generation of magnetoencephalography: Room temperature measurements using optically-pumped magnetometers. *NeuroImage*, 149:404 – 414.

Brinkmann, B. H., O'Brien, T. J., Dresner, M. A., Lagerlund, T. D., Sharbrough, F. W., and Robb, R. A. (1998). Scalp-recorded EEG localization in MRI volume data. *Brain Topography*, 10(4):245–253.

Budker, D. and Kimball, D. F. J. (2013). *Optical Magnetometry*. Cambridge University Press.

Budker, D. and Romalis, M. (2007). Optical magnetometry. *Nature Physics*, 3(4):227–234.

Colombo, A. P., Carter, T. R., Borna, A., Jau, Y.-Y., Johnson, C. N., Dagel, A. L., and Schwindt, P. D. D. (2016). Four-channel optically pumped atomic magnetometer for magnetoencephalography. *Opt. Express*, 24(14):15403–15416.

Dalal, S. S., Rampp, S., Willomitzer, F., and Ettl, S. (2014). Consequences of EEG electrode position error on ultimate beamformer source reconstruction performance. *Frontiers in Neuroscience*, 8(March):42.

Dale, A. M., Fischl, B., and Sereno, M. I. (1999). Cortical surface-based analysis. I. Segmentation and surface reconstruction. *NeuroImage*, 9(2):179–194.

Dale, A. M. and Sereno, M. I. (1993). Improved localizadon of cortical activity by combining EEG and MEG with MRI cortical surface reconstruction: a linear approach. *Journal of Cognitive Neuroscience*, 5(2):162–176.

Ettl, S., Rampp, S., Fouladi-Movahed, S., Dalal, S. S., Willomitzer, F., Arold, O., Stefan, H., and Häusler, G. (2013). Improved EEG source localization employing 3D sensing by "Flying Triangulation". *SPIE Optical Metrology 2013*, 87910V.

Fischl, B. (2012). FreeSurfer. *NeuroImage*, 62(2):774–781.

Fischl, B., Sereno, M. I., and Dale, A. M. (1999a). Cortical Surface-Based Analysis II: Inflation, Flattening, and a Surface-Based Coordinate System. *NeuroImage*, 9(2):195–207.

Fischl, B., Sereno, M. I., Tootell, R. B. H., and Dale, A. M. (1999b). High-resolution intersubject averaging and a coordinate system for the cortical surface. *Human Brain Mapping*, 8(4):272–284.

Goldenholz, D. M., Ahlfors, S. P., Hämäläinen, M. S., Sharon, D., Ishitobi, M., Vaina, L. M., and Stufflebeam, S. M. (2009). Mapping the signal-to-noise-ratios of cortical sources in magnetoencephalography and electroencephalography. *Human Brain Mapping*, 30(4):1077–1086.

Gramfort, A., Kowalski, M., and Hämäläinen, M. (2012). Mixed-norm estimates for the M/EEG inverse problem using accelerated gradient methods. *Physics in Medicine and Biology*, 57(7):1937–1961.

Gramfort, A., Luessi, M., Larson, E., Engemann, D. A., Strohmeier, D., Brodbeck, C., Parkkonen, L., and Hämäläinen, M. S. (2014). MNE software for processing MEG and EEG data. *NeuroImage*, 86:446–460.

Grave De Peralta Menendez, R., Hauk, O., Andino, S. G., Vogt, H., and Michel, C. (1997). Linear inverse solutions with optimal resolution kernels applied to electromagnetic tomography. *Human Brain Mapping*, 5(6):454–467.

Griffith, W. C., Knappe, S., and Kitching, J. (2010). Femtotesla atomic magnetometry in a microfabricated vapor cell. *Optics Express*, 18(26):27167–27172.

Hämäläinen, M. S., Hari, R., Ilmoniemi, R. J., Knuutila, J., and Lounasmaa, O. V. (1993). Magnetoencephalography—theory, instrumentation, and applications to noninvasive studies of the working human brain. *Reviews of Modern Physics*, 65(2):413–505.

Hämäläinen, M. S. and Ilmoniemi, R. J. (1994). Interpreting magnetic fields of the brain: minimum norm estimates. *Medical & Biological Engineering & Computing*, 32(1):35–42.

Haueisen, J., Ramon, C., Eiselt, M., Brauer, H., and Nowak, H. (1997). Influence of tissue resistivities on neuromagnetic fields and electric potentials studied with a finite element model of the head. *IEEE Transactions on Biomedical Engineering*, 44(8):727–735.

Hauk, O., Wakeman, D. G., and Henson, R. (2011). Comparison of noise-normalized minimum norm estimates for MEG analysis using multiple resolution metrics. *NeuroImage*, 54(3):1966–1974.

Hironaga, N., Hagiwara, K., Ogata, K., Hayamizu, M., Urakawa, T., and Tobimatsu, S. (2014). Proposal for a new MEG–MRI co-registration: A 3D laser scanner system. *Clinical Neurophysiology*, 125(12):2404–2412.

Huang, M. X., Shih, J. J., Lee, R. R., Harrington, D. L., Thoma, R. J., Weisend, M. P., Hanlon, F., Paulson, K. M., Li, T., Martin, K., Miller, G. A., and Canive, J. M. (2004). Commonalities and Differences among Vectorized Beamformers in Electromagnetic Source Imaging. *Brain Topography*, 16(3):139–158.

Iivanainen, J., Stenroos, M., and Parkkonen, L. (2017). Measuring MEG closer to the brain: Performance of on-scalp sensor arrays. *NeuroImage*, 147:542 – 553.

Jasper, H. H. (1958). The ten-twenty electrode system of the International Federation. *Electroencephalography and Clinical Neurophysiology*, 10(2):371–375.

Johnson, C. N., Schwindt, P. D. D., and Weisend, M. (2013). Multi-sensor magnetoencephalography with atomic magnetometers. *Physics in Medicine and Biology*, 58(17):6065.

Kamada, K., Sato, D., Ito, Y., Natsukawa, H., Okano, K., Mizutani, N., and Kobayashi, T. (2015). Human magnetoencephalogram measurements using newly developed compact module of high-sensitivity atomic magnetometer. *Japanese Journal of Applied Physics*, 54(2):026601.

Knappe, S., Alem, O., Sheng, D., and Kitching, J. (2016). Microfabricated Optically-Pumped Magnetometers for Biomagnetic Applications. *Journal of Physics: Conference Series*, 723:012055.

Knappe, S., Mhaskar, R., Preusser, J., Kitching, J., Trahms, L., and Sander, T. (2011). Chip-scale room-temperature atomic magnetometers for biomedical measurements. *IFMBE Proceedings*, 37:1330–1333.

Knappe, S., Sander, T., and Trahms, L. (2014). Optically-Pumped Magnetometers for MEG. In *Magnetoencephalography: From Signals to Dynamic Cortical Networks*, pages pp. 993–999. Springer Berlin Heidelberg.

Koessler, L., Cecchin, T., Caspary, O., Benhadid, A., Vespignani, H., and Maillard, L. (2011). EEG-MRI co-registration and sensor labeling using a 3D laser scanner. *Annals of Biomedical Engineering*, 39(3):983–995.

Koessler, L., Cecchin, T., Ternisien, E., and Maillard, L. (2010). 3D handheld laser scanner based approach for automatic identification and localization of EEG sensors. *2010 Annual International Conference of the IEEE Engineering in Medicine and Biology Society, EMBC'10*, pages pp. 3707–3710.

Koessler, L., Maillard, L., Benhadid, A., Vignal, J. P., Braun, M., and Vespignani, H. (2007). Spatial localization of EEG electrodes. *Neurophysiologie Clinique*, 37(2):97–102.

Kominis, I. K., Kornack, T. W., Allred, J. C., and Romalis, M. V. (2003). A subfemtotesla multichannel atomic magnetometer. *Nature*, 422(6932):596–599.

Kozinska, D., Carducci, F., and Nowinski, K. (2001). Automatic alignment of EEG/MEG and MRI data sets. *Clinical Neurophysiology*, 112(8):1553–1561.

Kozinska, D., Tretiak, O. J., Nissanov, J., and Ozturk, C. (1997). Multidimensional Alignment Using the Euclidean Distance Transform. *Graphical Models and Image Processing*, 59(6):373–387.

Lin, F. H., Witzel, T., Ahlfors, S. P., Stufflebeam, S. M., Belliveau, J. W., and Hämäläinen, M. S. (2006). Assessing and improving the spatial accuracy in MEG source localization by depth-weighted minimum-norm estimates. *NeuroImage*, 31(1):160–171.

Matsuura, K. and Okabe, Y. (1995). Selective minimum-norm solution of the biomagnetic inverse problem. *IEEE Transactions on Biomedical Engineering*, 42(6):608–615.

Mattout, J., Pélégrini-Issac, M., Garnero, L., and Benali, H. (2005). Multivariate source prelocalization (MSP): Use of functionally informed basis functions for better conditioning the MEG inverse problem. *NeuroImage*, 26(2):356–373.

Meyer, S. S., Bonaiuto, J., Lim, M., Rossiter, H., Waters, S., Bradbury, D., Bestmann, S., Brookes, M., Callaghan, M. F., Weiskopf, N., and Barnes, G. R. (2017). Flexible head-casts for high spatial precision MEG. *Journal of Neuroscience Methods*, 276:38–45.

Molins, A., Stufflebeam, S. M., Brown, E. N., and Hämäläinen, M. S. (2008). Quantification of the benefit from integrating MEG and EEG data in minimum l2-norm estimation. *NeuroImage*, 42(3):1069–1077.

Murthy, S. V. K., MacLellan, M., Beyea, S., and Bardouille, T. (2014). Faster and improved 3-D head digitization in MEG using Kinect. *Frontiers in Neuroscience*, 8(OCT):1–7.

Nurminen, J., Taulu, S., and Okada, Y. (2008). Effects of sensor calibration, balancing and parametrization on the signal space separation method. *Physics in Medicine and Biology*, 53(7):1975–1987.

Öisjöen, F., Schneiderman, J. F., Figueras, G. A., Chukharkin, M. L., Kalabukhov, A., Hedström, A., Elam, M., and Winkler, D. (2012). High-Tc superconducting quantum interference device recordings of spontaneous brain activity: Towards high-Tc magnetoencephalography. *Applied Physics Letters*, 100(13):132601.

Ou, W., Hämäläinen, M. S., and Golland, P. (2009). A distributed spatio-temporal eeg/meg inverse solver. *NeuroImage*, 44(3):932–946.

Russell, G. S., Eriksen, K. J., Poolman, P., Luu, P., and Tucker, D. M. (2005). Geodesic photogrammetry for localizing sensor positions in dense-

array *EEG*. *Clinical Neurophysiology*, 116(5):1130–1140.
Sander, T. H., Preusser, J., Mhaskar, R., Kitching, J., Trahms, L., and Knappe, S. (2012). Magnetoencephalography with a chip-scale atomic magnetometer. *Biomedical Optics Express*, 3(5):981.
Ségonne, F., Dale, A. M., Busa, E., Glessner, M., Salat, D., Hahn, H. K., and Fischl, B. (2004). A hybrid approach to the skull stripping problem in MRI. *NeuroImage*, 22(3):1060–1075.
Shah, V., Knappe, S., Schwindt, P. D. D., and Kitching, J. (2007). Subpicotesla atomic magnetometry with a microfabricated vapour cell. *Nature Photonics*, 1(11):649–652.
Shah, V. K. and Wakai, R. T. (2013). A compact, high performance atomic magnetometer for biomedical applications. *Physics in Medicine and Biology*, 58(22):8153–8161.
Stenroos, M. and Hauk, O. (2013). Minimum-norm cortical source estimation in layered head models is robust against skull conductivity error. *NeuroImage*, 81:265–272.
Stenroos, M. and Nummenmaa, A. (2016). Incorporating and Compensating Cerebrospinal Fluid in Surface-Based Forward Models of Magneto- and Electroencephalography. *PLoS ONE*, 11(7):e0159595.
Stenroos, M. and Sarvas, J. (2012). Bioelectromagnetic forward problem: isolated source approach revis(it)ed. *Physics in Medicine and Biology*, 57(11):3517–3535.
Taulu, S. and Kajola, M. (2005). Presentation of electromagnetic multichannel data: The signal space separation method. *Journal of Applied Physics*, 97(12).
Troebinger, L., López, J. D., Lutti, A., Bradbury, D., Bestmann, S., and Barnes, G. (2014). High precision anatomy for MEG. *NeuroImage*, 86:583–591.
Uutela, K., Hämäläinen, M., and Somersalo, E. (1999). Visualization of magnetoencephalographic data using minimum current estimates. *NeuroImage*, 10(2):173–180.
Van Veen, B., van Drongelen, W., Yuchtman, M., and Suzuki, A. (1997). Localization of brain electrical activity via linearly constrained minimum variance spatial filtering. *IEEE Transactions on Biomedical engineering*, 44(9):867–880.
Wang, Y. and Gotman, J. (2001). The influence of electrode location errors on EEG dipole source localization with a realistic head model. *Clinical Neurophysiology*, 112(9):1777–1780.
Whalen, C., Maclin, E. L., Fabiani, M., and Gratton, G. (2008). Validation of a method for coregistering scalp recording locations with 3D structural MR images. *Human Brain Mapping*, 29(11):1288–1301.
Xia, H., Ben-Amar Baranga, A., Hoffman, D., and Romalis, M. V. (2006). Magnetoencephalography with an atomic magnetometer. *Applied Physics Letters*, 89(21):211104.